MEASURING THE DIFFUSE OPTICAL LIGHT IN ABELL 1651

ANTHONY H. GONZALEZ,[1] ANN I. ZABLUDOFF,[2,3] DENNIS ZARITSKY,[2,3] AND JULIANNE J. DALCANTON[4]
Received 1999 December 18; accepted 2000 January 28

ABSTRACT

Using drift-scan data, a new approach to determining surface brightness profiles, and techniques for detecting low surface brightness signals, we fit the light profile of the brightest cluster galaxy (BCG) in the rich cluster Abell 1651 out to 670 h^{-1} kpc. This radius is a significant fraction of the virial radius of the cluster (2 h^{-1} Mpc), indicating that the sizes of the BCG and the cluster are comparable. We find that the profile is consistent with a de Vaucouleurs profile over the radial range probed. We also find that the integrated light profile of the BCG in Abell 1651 contributes 36% of the total cluster light within 500 h^{-1} kpc. Including all luminous components, we obtain $M/L_I \sim 160\ h$ for the cluster, which would be overestimated by $\sim 20\%$ without the BCG halo. Furthermore, the relatively red color of the BCG at large radii suggests that recent disruption and tidal stripping of spirals and dwarf ellipticals do not contribute significantly to the halo luminosity. The color and the form of the profile are consistent with a scenario in which the BCG forms from filamentary collapse during the epoch of cluster formation, with relatively little evolution in the past 5 Gyr. We remove the BCG and other detected galaxies from the image and construct a two-dimensional surface brightness map of the cluster core. Several knots of excess emission are found, but the total diffuse component is constrained to contribute less than 5% of the cluster light.

Subject headings: galaxies: clusters: general — galaxies: clusters: individual (Abell 1651) — galaxies: formation — galaxies: structure — techniques: image processing

1. INTRODUCTION

Measuring the surface brightness profiles of brightest cluster galaxies (BCGs) out to large radii is critical both for understanding the formation of these giant galaxies and for determining the mass-to-light ratios (M/L) of galaxy clusters. First, the form and color of the profiles yield information about the dynamical state and the distribution of stellar populations (Malamuth & Richstone 1984; Merritt 1984; Schombert 1988; Andreon, Garilli, & Maccagni 1995; Dubinski 1998), thus constraining the accretion history of these systems. Second, measurement of the light contributed by the extended profile of the BCG is required for an accurate determination of the total cluster luminosity, which is essential for deriving an unbiased M/L.

Despite the importance of accurate BCG profile measurements, recent determinations disagree. For example, from a large sample of BCGs Schombert (1986) finds that some of these galaxies have a "cD halo"—an extended component, centered on the BCG, with a significantly different surface brightness profile than the central region of the galaxy. Graham et al. (1996) find instead that BCGs can be fit with single Sersic (1968) profiles; with observed profiles that are typically shallower than a de Vaucouleurs ($r^{1/4}$) law. Meanwhile, the few detailed analyses of diffuse light in individual clusters find BCGs that are well described by $r^{1/4}$ law profiles. Uson, Bough, & Kuhn (1990, 1991) show that the radial profile of the brightest cluster galaxy in Abell 2029 is consistent with a de Vaucouleurs model (reduced $\chi^2 = 0.78$ in R) out to $r \equiv (ab)^{1/2} = 425\ h^{-1}$ kpc, and Scheick & Kuhn (1994) conclude that the BCG in Abell 2670 has an $r^{1/4}$ profile (reduced $\chi^2 = 0.28$ in V) out to 230 h^{-1} kpc. The latter result is surprising given that this giant elliptical is classified by both Oemler (1973) and Schombert (1986) as a cD galaxy with a pronounced envelope starting at $r \sim 80\ h^{-1}$ kpc.

To unambiguously constrain BCG formation and permit accurate M/L determination, we aim to resolve this disagreement in the form of BCG luminosity profiles. A new study is needed that extends the detailed analysis techniques used in Abell 2029 and 2670 to a statistical sample of clusters. However, attaining the required flat-fielding accuracy with pointed CCD observations is a computationally and observationally intensive task (Gudehus 1989; Uson et al. 1990, 1991; Scheick & Kuhn 1994). In this paper we develop a method of studying the diffuse light that minimizes the required telescope time and can be used to efficiently study a large sample of clusters. We employ very flat drift-scan data, a new approach to determining surface brightness profiles, and techniques for detecting low surface brightness signals that, having been developed for finding high-redshift clusters (Dalcanton 1996; Zaritsky et al. 1997), are also applicable to this problem.

With these tools, we perform a detailed analysis of the distribution of light in the cluster Abell 1651 at $z = 0.084$. We choose this cluster to be our first because it appears to be dynamically relaxed and hence is a good system with which to test our method. Specifically, X-ray observations show a symmetric temperature profile cocentric with the brightest cluster galaxy, with a mean temperature $T_X = 6.1$ keV (Markevitch et al. 1998). We focus on measuring the surface brightness profile of the BCG, constraining the luminosity contribution of diffuse light, and assessing the relative contributions of various components to the total cluster luminosity.

[1] Postal address: Department of Astronomy and Astrophysics, University of California at Santa Cruz, Santa Cruz, CA 95064.

[2] University of California Observatories/Lick Observatory and Department of Astronomy and Astrophysics, University of California at Santa Cruz, Santa Cruz, CA 95064.

[3] Steward Observatory, University of Arizona, 933 North Cherry Avenue, Tucson, AZ 85721.

[4] Department of Astronomy, University of Washington, Box 351580, Seattle, WA 98195-1580.

2. DATA AND PRELIMINARY REDUCTIONS

Drift-scan data were obtained using the Las Campanas 1 m telescope, the Great Circle Camera (Zaritsky, Schectman, & Bredthauer 1996), and the Tek5 CCD with both the Gunn i filter (transformed to Cousins I using Landolt standards) and a wideband filter (hereafter W) that roughly covers the wavelength region between B and I (see Fig. 1). This W filter is designed to maximize the incident signal while avoiding sky emission lines in the red and atmospheric refraction in the blue. Individual drift scans are $2048 \times 13,000$ pixels with a plate scale of $0\rlap{.}''7$ pixel^{-1} and an effective exposure time of 95 s. The total time required for a single scan, including the time spent off-source, is ~ 10 minutes. We have three scans of the cluster core in I and two in W, for total exposure times of 4.75 minutes in I and 3.17 minutes in W. Conditions during the observations were photometric, with seeing of $1\rlap{.}''5$.

A key property of the data is the intrinsic flatness of drift scans. The data must have residual flatness variation less than 0.5% or these variations will be the dominant source of noise in our derived surface brightness map. In drift scans, pixel-to-pixel variation is minimized as data are clocked across the chip, so sensitivity variations are a concern only perpendicular to the readout direction (at a level $\sim 2\%$ in our raw data). Consequently, we construct a one-dimensional flat field, for which the Poisson noise is reduced significantly relative to a two-dimensional flat field. Flat-fielding is accomplished in two stages. In both stages we use a set of six (W) or seven (I) data scans, to construct a median averaged flat field. Each scan is 13,000 pixels in length and the typical sky level in I is ~ 140 counts, so the associated Poisson noise is 0.03% per column. The first stage of flat-fielding immediately follows bias subtraction and reduces sensitivity variation from 2% to 0.2%. This level is below the noise from other sources; however, the remaining variation due to the presence of objects in the scans is correlated across columns. The second flat-fielding

stage is designed to remove this residual variation. To eliminate contamination from resolved objects, we use the segmentation image generated by SExtractor version 2.0.15 (Bertin & Arnouts 1996) to generate a binary mask. We convolve this binary mask with a boxcar filter to mask all pixels within 7″ of object detection regions. The second-stage flat-field image is constructed using only the unmasked pixels. Subsequent to this final flat-fielding, all scans are flat to less than 0.1%, which corresponds to $\mu_I = 28.4$ mag arcsec^{-2}, and any residual column-column variation is not discernible.

Similar to the sensitivity variation, temporal sky variability is a one-dimensional problem with drift-scan data. This variability is a smooth feature with maximum amplitude of $\sim 10\%$ of the sky level over the length of a scan. We apply a median boxcar of size 700″ (1000 pixels or 855 h^{-1} kpc) to a flat-fielded version of each image in which all resolved objects are masked. We find that a filter of this size does not cause oversubtraction of the sky near the cluster core or bright stars. The entire region within 350″ (500 pixels) of the cluster core is also masked as a precaution. We also try an alternative method in which the sky is fit with a spline of order 5. Comparison of the two methods yields rms variations at a level of $\mu_I \sim 28$ mag arcsec^{-2} and uncertainty at the level of $\mu_I \sim 30.5$ mag arcsec^{-2} in fitting the profile of the brightest cluster galaxy.

Following bias subtraction, flat-fielding, and sky subtraction, we register all images. The I- and W-band data are averaged to generate a single image for each band, and we also add the data from both bands to maximize the signal available for tracing the BCG profile at large radii. Adding the images also reduces uncertainty from removal of the time variable sky component.

3. THE CLUSTER COMPONENTS

To identify and characterize all significant sources of luminosity in the core of the cluster, we proceed as follows. First, we model the brightest cluster galaxy to determine the form of its surface brightness profile (§ 3.1). Next, we remove the brightest cluster galaxy and all other detected objects from the image and analyze the distribution of light from diffuse matter and faint, undetected cluster galaxies (§ 3.2). Finally, we use this information to assess the relative contribution of each of these components to the total cluster luminosity (§ 3.3).

3.1. *The Brightest Cluster Galaxy*

We model the brightest cluster galaxy using the IRAF routine ELLIPSE.[5] SExtractor is again used to generate an object mask. Previous work has demonstrated that contamination from other sources can significantly bias the derived profile at low surface brightness levels (Uson et al. 1990, 1991; Porter, Schneider, & Hoessel 1991), and so we mask all objects except the BCG and all pixels within 10″ of object detection regions. This procedure eliminates 30% of the image data from further consideration by ELLIPSE. The masking is then augmented by manual masking of regions near saturated stars and bright galaxies, which
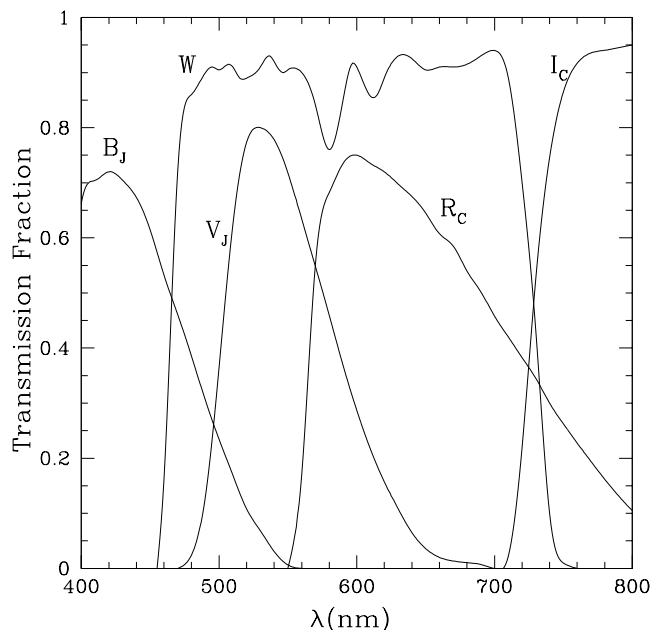
FIG. 1.—Comparison of the broad W filter utilized in this work to standard Johnson (BV) and Cousins (RI) filters. The red cutoff is designed to avoid night sky lines while maximizing incident flux.
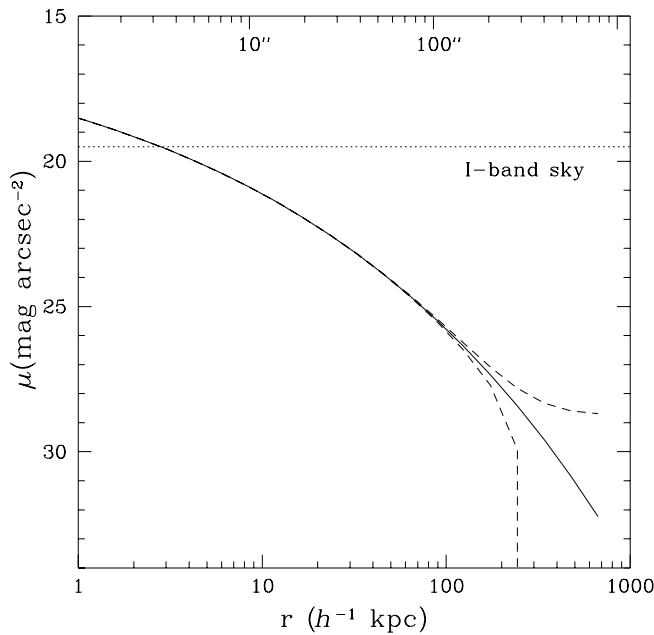
FIG. 2.—The effect of a 0.01% error in the sky level (comparable to our observations) on an initial de Vaucouleurs profile. Error in sky estimation can lead to either truncation of the profile or an artificial excess of light.

excludes an additional 15% of the pixels in the image.[6] Our approach is similar to that utilized by Vilchez-Gómez, Pelló, & Sanahuja (1994) in their study of the diffuse light of Abell 2390. We generate best-fit models for the BCG, with position angle and ellipticity first allowed to vary freely and then with these parameters fixed to the values given by SExtractor. The resultant surface brightness profile, as a function of $r = (ab)^{1/2}$, is unchanged whether these parameters are fixed or allowed to vary. We choose to fix both parameters.

To measure the surface brightness profile of the BCG at large radii, an accurate determination of the sky level is critical. Figure 2 illustrates the effect on an intrinsic de Vaucouleurs profile of error in determination of the sky level. Such an error in the background leads either to the truncation of the profile or to the existence of an artificial envelope. As has been noted by a number of authors (de Vaucouleurs & de Vaucouleurs 1970; Oemler 1976; Melnick, Hoessel, & White 1977; Uson et al. 1990, 1991), systematic errors in the measured sky level can be induced by intrinsic background variation, spatial variation in detector response (e.g., flatness variation for CCDs), and contamination from the outer halos of other cluster members. For this data set we calculate that the uncertainty in our sky determination is 0.01% ($\sigma_{\rm sky} \sim 29.5$ mag arcsec^{-2} in I), which will impact the form of the profile at $r > 200$ h^{-1} kpc. To unambiguously quantify the form of the profile at larger radii, we must employ a technique that is insensitive to the level of background light.

Our alternate method uses the differential change in the flux, Δf, between points in the profile. By taking a differential measurement, we obtain a quantity that is independent of a constant background level but still contains all the

information present in the luminosity profile. One difficulty exists with this approach. If we compute the differential change only for radially adjacent surface brightness measurements ($\Delta f_i \equiv f_i - f_{i+1}$), then both the reduced χ^2 (χ^2_v) and the error bars for the model parameters are dependent on radial sampling density. Higher sampling density leads to lower χ^2_v and larger error bars on the model parameters because the flux difference between adjacent points decreases while the associated uncertainty does not.

Our preferred method, described in the Appendix, is to compute for each point the flux difference relative to all points at larger radii. We define

$$\Delta f_i \equiv f_i - \frac{1}{N-i} \sum_{j=i+1}^{N} f_j \qquad (1)$$

and compare this quantity with model predictions. This approach removes the dependence of χ^2_v upon sampling density, permitting robust determination of both model parameters and their associated uncertainties.

Using ELLIPSE we measure the profile of the BCG in Abell 1651 out to $r = 670$ h^{-1} kpc. Beyond this radius, the angular extent of the elliptical annulus used to measure the profile exceeds the width of the image. We show in Figure 3a the flux differential in $I + W$ for the BCG in Abell 1651 and our best-fit de Vaucouleurs model. A best-fit Sersic (1968) model and a model with a cD envelope are also shown in the residual plot, Figure 3b.[7] The de Vaucouleurs model fit to the differential profile has $r_e = 41.7 \pm 0.8$ h^{-1}

---

[7] The properties of the cD envelope are equivalent to the envelope observed by Schombert (1988) for Abell 2670. It is modeled with a de Vaucouleurs profile with $r_e = 330$ h^{-1} kpc and $\Sigma_e = 0.008\Sigma_{e,\rm galaxy}$.
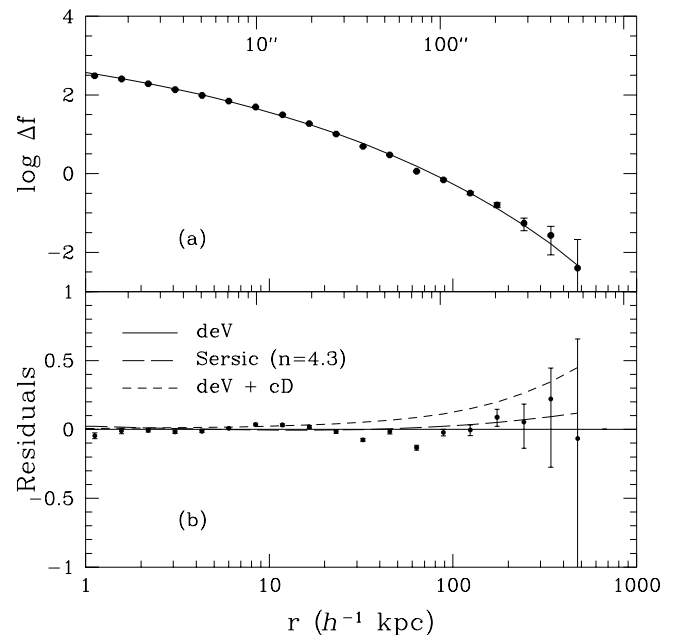

FIG. 3.—(a) Flux differential as a function of radius, with Δf defined as in eq. (1). The solid line is the best-fitting de Vaucouleurs model ($r_e = 41.7$ h^{-1} kpc). (b) Residual plot for the upper graph showing variation about the model fit. Also shown are the optimal $n = 4.3$ Sersic model (*long-dashed line*) and a model with a de Vaucouleurs galaxy plus a de Vaucouleurs cD envelope with $r_e = 330$ h^{-1} kpc and $\Sigma_e = 0.008\Sigma_{e,\rm galaxy}$ (*short-dashed line*).

---

[6] The regions of excess surface brightness described in § 3.2 are also masked at this point and so are not responsible for any observed structure in the profile.

kpc (68% confidence) with $\chi_v^2 = 13.7$. The large χ_v^2 is due to radial oscillations in the light profile (see Fig. 3b), which is seen in both filters. This radial structure is not due to using a fixed position angle and eccentricity; the same oscillations are seen when these parameters are permitted to vary. The best-fit Sersic model formally has $n = 4.3 \pm 0.2$ with $\chi_v^2 = 14.3$, which is slightly shallower than a de Vaucouleurs model. However, the oscillations seen in the residuals may contribute to this result. For example, if the three points beyond 300 h^{-1} kpc (which appear to be on a rising part of the oscillation pattern) are excluded from the fit, then the best-fit model has $n = 3.9$, and so we conclude that the Sersic index of the galaxy profile is consistent with $n = 4$ (de Vaucouleurs) to within our observational uncertainty. We also note that the cD envelope model shown in Figure 3b yields $\chi_v^2 = 21.6$.

Figure 4 shows the $I + W$ composite surface brightness profile of the BCG in Abell 1651, with the background level fixed using the results from the differential analysis and the vertical scale set such that $\mu(1\ h^{-1}\ \mathrm{kpc}) = 0$ mag arcsec^{-2} (see also Table 1). The de Vaucouleurs, Sersic, and cD envelope models shown are the same as in Figure 3. A fit to the stellar point-spread function is also overlaid for comparison, demonstrating that seeing has a negligible impact on the profile. Figure 5 shows the I- and W-band profiles independently, and de Vaucouleurs fits, with the effective radius fixed to $r_e = 41.7\ h^{-1}$ kpc. Error bars represent observed rms flux variations in the data and do not include systematic errors. For $r_e = 41.7\ h^{-1}$ kpc, independent fits in the I and W bands respectively yield $\mu_e(I) = 23.55$ mag arcsec^{-2} with $\chi_v^2 = 9.4$ and $\mu_e(W) = 24.70$ mag arcsec^{-2} with $\chi_v^2 = 14.7$.
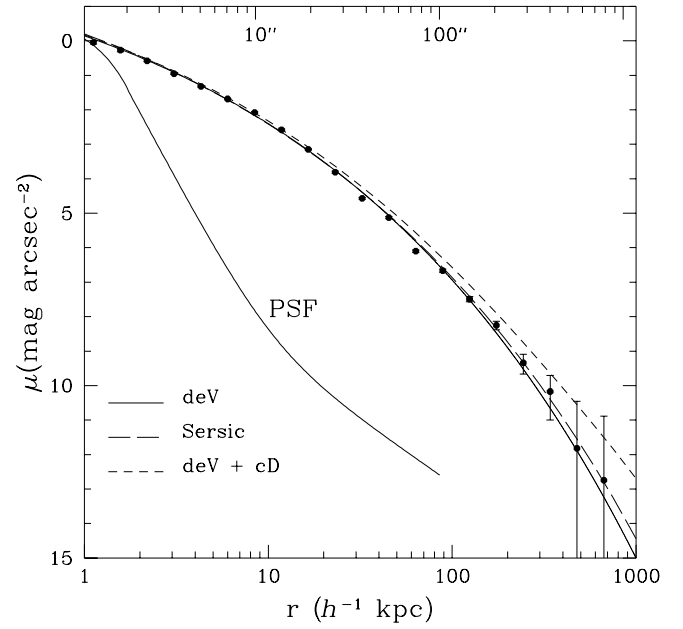

FIG. 4.—Composite $I + W$ surface brightness profile. The lines are the same models as in Fig. 3.

In addition to measuring the form of the profile, we also test for the presence of a color gradient. While we are able to measure the profiles out to $r \sim 500\ h^{-1}$ kpc in both bands, for $r > 100\ h^{-1}$ kpc we are wary of systematic errors that may bias the resultant colors. Consequently, we restrict

TABLE 1
SURFACE BRIGHTNESS PROFILE DATA

r^a (arcsec)	r (h^{-1} kpc)	$I+W^b$ (mag arcsec^{-2})	I (mag arcsec^{-2})	W (mag arcsec^{-2})
0.65	0.80	-0.09 ± 0.04	18.58 ± 0.04	19.72 ± 0.04
0.92	1.12	0.05 ± 0.04	18.71 ± 0.05	19.85 ± 0.04
1.28	1.57	$0.27^{+0.05}_{-0.04}$	18.93 ± 0.05	20.07 ± 0.04
1.79	2.19	0.58 ± 0.03	19.24 ± 0.03	$20.38^{+0.02}_{-0.03}$
2.51	3.07	0.95 ± 0.02	$19.61^{+0.03}_{-0.02}$	20.76 ± 0.02
3.52	4.30	1.32 ± 0.02	19.98 ± 0.02	21.12 ± 0.01
4.92	6.01	1.69 ± 0.01	20.34 ± 0.01	21.5 ± 0.01
6.89	8.42	2.08 ± 0.02	20.74 ± 0.02	21.88 ± 0.02
9.65	11.79	2.58 ± 0.02	21.24 ± 0.02	22.38 ± 0.02
13.51	16.50	3.15 ± 0.02	21.80 ± 0.02	22.96 ± 0.02
18.91	23.10	3.81 ± 0.03	22.47 ± 0.04	23.61 ± 0.03
26.47	32.34	4.57 ± 0.02	23.18 ± 0.03	24.42 ± 0.02
37.06	45.28	$5.13^{+0.04}_{-0.03}$	23.74 ± 0.04	24.98 ± 0.03
51.88	63.39	$6.10^{+0.04}_{-0.03}$	24.69 ± 0.06	26.01 ± 0.04
72.64	88.74	6.67 ± 0.05	$25.24^{+0.07}_{-0.06}$	26.59 ± 0.06
101.69	124.24	7.49 ± 0.08	$26.14^{+0.11}_{-0.10}$	27.38 ± 0.08
142.37	173.93	$8.25^{+0.13}_{-0.12}$	$26.79^{+0.18}_{-0.15}$	$28.21^{+0.15}_{-0.13}$
199.31	243.51	$9.34^{+0.33}_{-0.25}$	$28.02^{+0.50}_{-0.34}$	$29.78^{+0.73}_{-0.43}$
279.04	340.92	$10.17^{+0.83}_{-0.46}$	$28.71^{+1.47}_{-0.60}$	$30.81^{+\infty}_{-0.78}$
390.66	477.28	$11.82^{+\infty}_{-1.37}$	$< 29.55^c$	$31.14^{+\infty}_{-1.00}$
546.93	668.20	$12.74^{+\infty}_{-1.86}$	...	...

^{a} The seeing during these observations was 1″5, and so data at smaller radii do not reflect the true profile of the galaxy.

^{b} The values given for $I + W$ have been arbitrarily normalized such that $\mu(1\ h^{-1}\ \mathrm{kpc}) = 0$ mag arcsec^{-2}.

^{c} At this radius the I-band flux was indistinguishable from the background level, and so we are only able to place a lower bound on the magnitude.
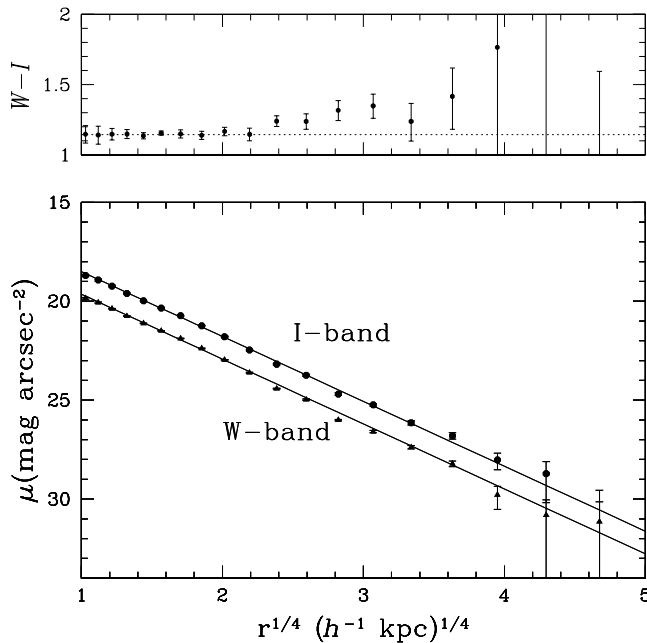
Fig. 5.—Top: BCG color as a function of radius. A mild reddening is evident from 20 to 100 h^{-1} kpc. At larger radii, the derived color is sensitive to the background level and so should be viewed with caution. Bottom: I-band (circles) and W-band (triangles) surface brightness profiles. Solid lines are best-fit models as in Fig. 4.

our attention to the inner 100 h^{-1} kpc. We find a mild gradient in the profile [$\Delta(W-I)/(\Delta \log r) = 0.25 \pm 0.08$] from 15 to 100 h^{-1} kpc, with the halo at 100 h^{-1} kpc redder than the center of the BCG by 0.2 mag. This mild gradient is consistent with other studies that have found shallow or no color gradients in BCGs (Mackie 1992; Garilli et al. 1997). For comparison, in their study of 17 non-BCG elliptical galaxies ($-22.5 < M_B < -20$), Franx, Illingworth, & Heckman (1989) find in the mean a slightly blue radial gradient [$\Delta(B-R)/(\Delta \log r) \sim -0.1$].

The color gradient of the BCG is a potentially valuable probe of the evolutionary history of the system. Qualitatively, if significant recent accretion of cluster galaxies has occurred in the halo, then we should expect the halo to be blue relative to the core of the BCG, independent of whether the accreted systems are spirals or ellipticals. Spirals are bluer because of ongoing star formation, while the relative blueness of fainter ellipticals is primarily a metallicity effect (Larson 1974; Kauffmann & Charlot 1998; Ferreras, Charlot, & Silk 1999). For reference, we estimate that if one $\sim L_*$ spiral ($\sim 5\%$ of the total luminosity of the BCG) is accreted within the past 2 Gyr and deposited uniformly at $50 < r < 100$ h^{-1} kpc, the halo at these radii will be ~ 0.1 mag bluer after accretion. Conversely, for formation scenarios in which there is no significant, recent contribution to the outer halo from tidally disrupted systems, we expect either no gradient or a mild red gradient if there has been subsequent star formation in the center of the galaxy. One such formation scenario is demonstrated by Dubinski (1998) in a simulation that also produces a de Vaucouleurs profile for the BCG. Unfortunately, quantitative model predictions are currently lacking, and so while our observations qualitatively agree with the early formation scenario, further modeling is needed for confirmation.

3.2. The Cluster Surface Brightness Distribution

Is there a discernible presence of intracluster light that is not associated/cocentric with the BCG? To investigate this issue, we first subtract from the image the BCG using our model from § 3.1 and all other galaxies with I-band isophotal areas larger than 175 pixels using the IRAF package GIM2D (Simard 1998; Marleau & Simard 1998). GIM2D generates optimal bulge + disk fits for each object, with an exponential disk and de Vaucouleurs profile bulge. The motivation for this detailed approach is to remove not only the visible central regions of these galaxies but also their contribution to the total cluster light at fainter surface brightness levels.

Subsequent to the application of GIM2D, we use FOCAS (Jarvis & Tyson 1981; Valdes 1993[8]) to remove all remaining detected objects with $m_I < 21$ (or $m_W < 22.8$) and replace them with locally drawn, random sky pixels. The interior regions of the previously removed bright galaxies are also replaced by locally drawn, random sky pixels as a precaution against residual galactic light contaminating the cluster surface brightness map. At this stage, we also mask bright stars and the inner 35″ of the BCG. Next, we convolve the cleaned image with a 10″ (12.2 h^{-1} kpc) exponential kernel to generate a smoothed two-dimensional map of the core region of the cluster. This kernel size is chosen as a compromise between sensitivity and resolution, being sufficiently small to resolve individual cluster galaxies but wide enough to probe to $\mu > 26$ mag arcsec^{-1}. Residual variations persist after smoothing at an approximate rms level $\mu_I = 26.65$ mag arcsec^{-2}, and we detect fluctuations down to $\mu_I \sim 26$ mag arcsec^{-2}. Figure 6 illustrates the process used to generate the surface brightness map. For comparison, the bottom panel, in which the brightest cluster galaxy halo is not removed, is included.

We find that within a radius of 400 h^{-1} Mpc of the BCG there exist three regions of excess brightness with peak surface brightnesses[9] $\mu_I < 25.75$ mag arcsec^{-2}. These regions are denoted as A, B, and C in the middle right panel of Figure 6. An additional ring of excess brightness can also be seen at the bottom of the panel surrounding a masked star, but this ring is due to the extended point-spread function of the star. Other regions of excess brightness can also be seen, such as the one between the BCG and the bright star, but these fall below our $\mu_I = 25.75$ mag arcsec^{-2} threshold. Of the three peaks, B is the brightest and largest, with a peak surface brightness $\mu_I = 25.3$ mag arcsec^{-2}. The total excess luminosity from this region corresponds to $L_I = (1.4 \pm 0.5) \times 10^{10} L_\odot$. Region B is aligned with the semimajor axis of the BCG (see Fig. 6).

To discern whether these enhancements are diffuse in origin, we look for evidence of faint galaxies coincident with the bright regions. In region B, the detected faint galaxy population cannot account for the excess flux. Coupled with its large angular size, this eliminates the possibility that the excess is due to a higher redshift group or cluster. This region is possibly the remnant of a tidally disrupted cluster

---

[8] The FOCAS User's Guide can be found at ftp://iraf.noao.edu/iraf/docs/focas/ as the gzipped file focasguide.ps.gz.

[9] Note that this is the peak surface brightness after convolution. The true peak surface brightnesses could be significantly brighter if the sources have spatial scales much smaller than the smoothing kernel (i.e., individual faint galaxies).
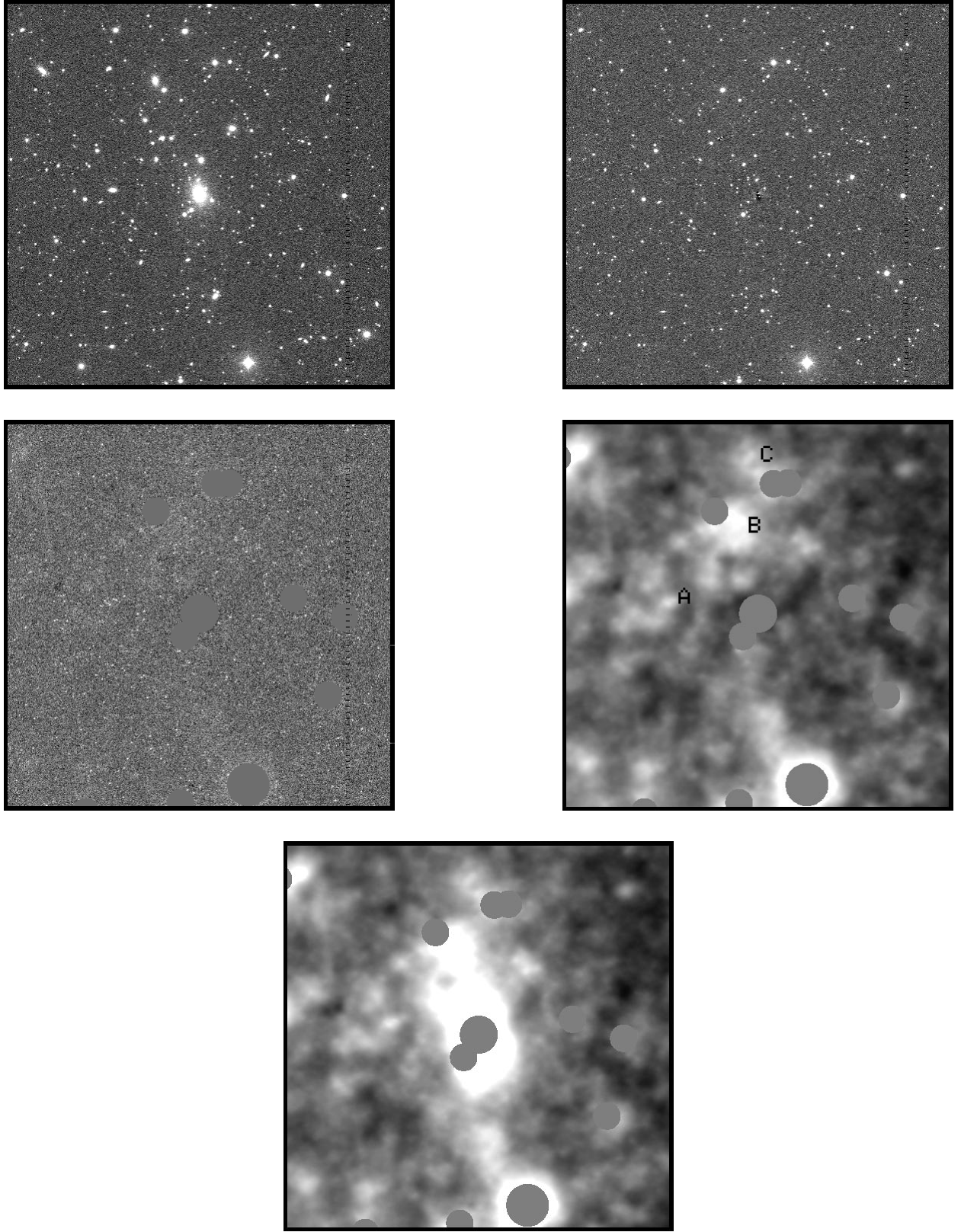
Fɪɢ. 6.—Sequence of I-band images illustrating the process used to generate the surface brightness map. Starting with the original image (*upper left*), first the BCG and brightest galaxies are modeled and removed (*upper right*). Next, all objects with $\mu_I < 21$ mag arcsec^{-2} are replaced with locally drawn sky pixels and masks are applied to the bright objects (*middle left*). Finally, this image is convolved with an exponential kernel to generate the surface brightness map (*middle right*). The most significant feature in the surface brightness map is the region marked B, which has a peak surface brightness of $\mu_I = 25.3$ mag arcsec^{-2}. For comparison, a surface brightness map is also shown in which the halo of the BCG is not modeled and removed (*bottom*). In all images, east is up and north is to the left. Each frame is $700''$ ($855\ h^{-1}$ kpc) on a side.

galaxy. Similar low surface brightness features have been seen in the Coma Cluster (Gregg & West 1998) and can be explained as arising from tidal processes. Alternately, this region could arise from a significant local enhancement of galaxies fainter than can be detected in our data. This interpretation seems less plausible because it would require an excess relative to the expected average cluster density of at least 20 galaxies fainter than our detection threshold, with no corresponding overdensity of galaxies brighter than the detection threshold.

Inspection of regions A and C (in contrast to region B) reveals a group of faint galaxies associated with each surface brightness excess. These galaxies have $m_I > 21$ mag arcsec^{-2} and so were not removed from the image by FOCAS prior to smoothing. In both cases the flux associated with the fluctuation can be accounted for by light from these faint galaxies. Such groups could be either clumped dwarf galaxies associated with the cluster or more distant clusters or groups. Based on the work of Gonzalez et al. (2000) detecting distant clusters, the surface density of background clusters is such that ~ 1 would be detected in this field and so is consistent with the latter explanation. To constrain the origin of fluctuations A and C, we measure the $W - I$ color of the associated faint galaxies. These galaxies are shown in Figure 7 and compared to the color-magnitude relation for the cluster, derived using galaxies with $m_W < 20$ (dashed line). The weighted mean color of the ensemble is $W - I = 0.97$ (~ 0.3 mag bluer than the core of the BCG), which corresponds to $R - I \sim 0.58$. This color is consistent with the galaxies being dwarf ellipticals in the cluster and inconsistent with their being giant ellipticals at higher redshift. Based on color alone, however, we cannot rule out the possibility that these galaxies are clustered spirals at higher redshift. If these are indeed cluster dwarfs, it is unclear why they are tightly clustered apart from any bright cluster galaxies.

TABLE 2
ABELL 1651 *I*-BAND LUMINOSITY BUDGET

Source	$h^{-2} L_\odot$	Fraction of Light (%)
Brightest cluster galaxy	1.2×10^{12}	36
Luminosity function ($m < 20.5$)	2.1×10^{12}	62
LF($m > 21$) + other diffuse light	7×10^{10}	2

3.3. *Relative Luminosity Contributions*

In § 3.2 we found that a de Vaucouleurs profile with a total luminosity of $L_I = 1.17 \times 10^{12} \, h^{-2} \, L_\odot$ is a good fit to the BCG light profile.[10] To assess the fractional contribution of the BCG to the total cluster light, we examine the region within $r = 500 \, h^{-1}$ kpc of the center of the BCG. As mentioned earlier, the location of the BCG is consistent with the kinematic center of the cluster as defined by X-ray data. Roughly 98% of the luminosity of the central galaxy is contained within this radius. We calculate the total luminosity from cluster galaxies with $m_I < 20.5$ within the same region. Statistical background subtraction is used to correct for the contribution of galaxies not associated with the cluster. We use the region of the image farther than $2 \, h^{-1}$ Mpc from the cluster core, covering an area of 0.58 deg^2, to compute the average off-cluster contribution. The integrated flux for galaxies with $m_I < 20.5$ is computed in both cluster and off-cluster regions, with background subtraction resulting in a 25% reduction in the observed cluster flux. The summed, extinction-corrected luminosity of cluster galaxies, excluding the BCG, is $L_I = 2.1 \times 10^{12} \, L_\odot$.

To estimate the luminosity of cluster galaxies or intracluster light below this magnitude level, we use the surface brightness map (middle right in Fig. 6). We cannot discern whether light in the surface brightness map is due to faint galaxies or diffuse intracluster light but instead place an upper bound on the combined contribution by summing the total residual light within the same $r = 500 \, h^{-1}$ kpc elliptical region and background subtracting using an off-cluster region of the scan. To compute the mean off-cluster sky level, we use a region adjacent to this ellipse that extends 3000 pixels (35') in right ascension in both directions. The largest source of uncertainty in this measurement is due to large-scale residual gradients in the background sky level, generated primarily by scattered light from off-image stars. Including a conservative estimate for this uncertainty, we calculate an excess flux of 110^{+190}_{-110} counts s^{-1} within $r = 500 \, h^{-1}$ kpc, which corresponds to $L = 0.7^{+1.2}_{-0.7} \times 10^{11} \, h^{-2} \, L_\odot$, or 2^{+3}_{-2} % of the total cluster light in this region. Because the error bars are large, we are not able to place a meaningful constraint on the faint end of the luminosity function. All faint-end Schechter function slopes with $\alpha > -1.98$ for $m > 20.5$ are consistent with the observed flux to within 3 σ. Our data are shallow, but our observed luminosity function has an upturn at the faint end in both bands and a slope $|\alpha| \sim 1.7$–1.9. This measurement suggests that any excess light can be explained as arising from faint cluster galaxies.

Table 2 lists the total and fractional contributions of each component of the net cluster luminosity within 500 h^{-1} kpc. The central dominant elliptical is a key contributor to the
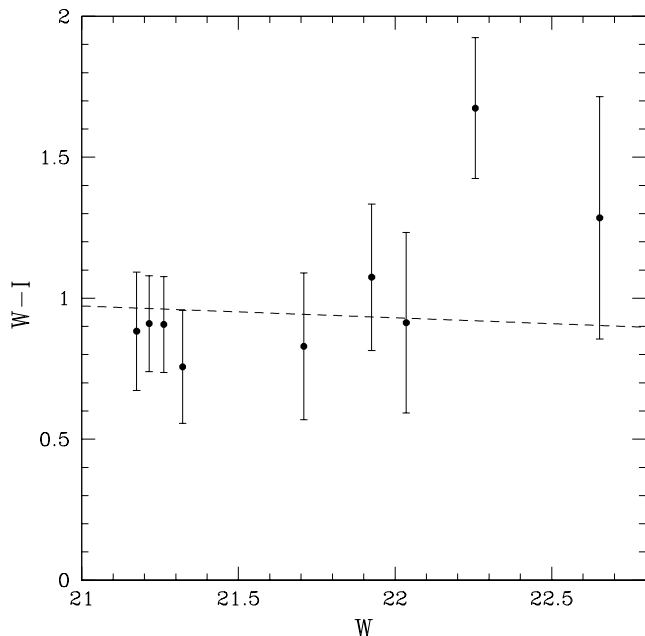

FIG. 7.—Color-magnitude diagram for the faint galaxies coincident with excess surface brightness regions A and C. The dashed line is the red sequence for the cluster constructed from galaxies with $m_W < 20$.

[10] The luminosity is corrected for a galactic extinction of 0.05 mag (Schlegel, Finkbeiner, & Davis 1998).
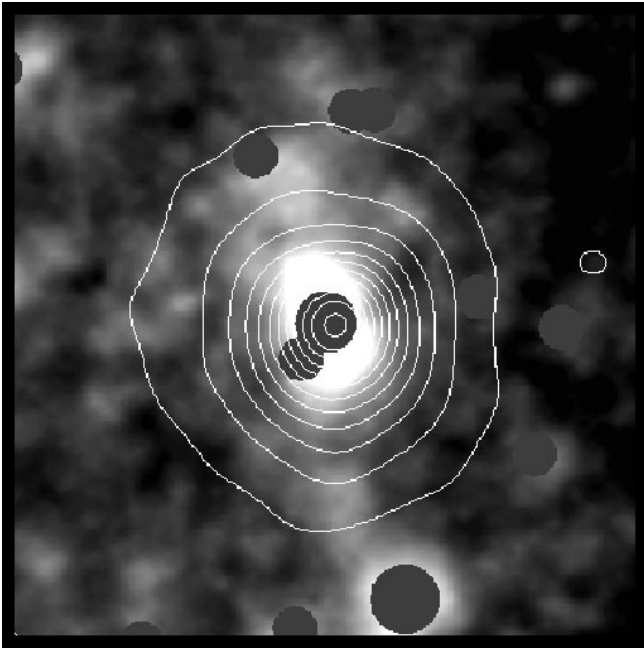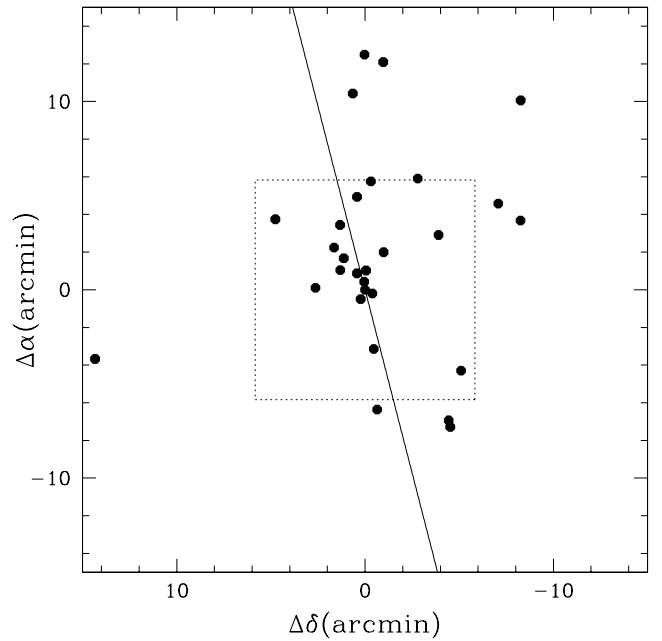
FIG. 8a

FIG. 8b

FIG. 8.—(a) X-ray contours overlaid on the smoothed image of the BCG halo. As in Fig. 6, the image is 855 h^{-1} kpc on a side. The X-ray image is from the *ROSAT* PSPC, with an exposure time of 7435 s. To generate the contours shown, the image is smoothed with a Gaussian of 30″ FWHM; the resulting map has a resolution of about 40″ (49 h^{-1} kpc). This resolution is determined from the FWHM of several point sources lying just outside the displayed field. The lowest contour level is $3 - \sigma$ above the background, and contour levels are displayed in $1 - \sigma$ increments. (b) Distribution of all spectroscopically confirmed members of the cluster that lie within a 15′ (1100 h^{-1} kpc) radius of the BCG. The confirmed members preferentially represent the bright end of the cluster luminosity function. The solid line indicates the position angle of the BCG. The inner box denotes the region displayed in Fig. 8a. East is up, north is to the left.

cluster luminosity. The BCG fractional contribution of 36% is in good agreement with the results from Uson et al. (1990, 1991) for Abell 2029 and Scheick & Kuhn (1994) for Abell 2670, who find that the BCGs contribute 23% of the cluster light within 780 h^{-1} kpc and 30% ± 8% of the total cluster light, respectively. Furthermore, as in Abell 2029 diffuse light beyond that associated with the BCG is a negligible contributor to the total light of this system.

4. THE MASS-TO-LIGHT RATIO

X-ray and optical spectroscopic data exist for Abell 1651, enabling us to determine the cluster mass and hence the *I*-band mass-to-light ratio. Markevitch et al. (1998) computed an emission-weighted temperature of 6.1 ± 0.4 keV (90% confidence) for the cluster. Girardi et al. (1998) computed a cluster velocity dispersion $\sigma = 1006^{+118}_{-96}$ km s^{-1}. Combining these two values yields

$$\beta \equiv \frac{\mu m_p \sigma^2}{kT} = 1.04 \pm 0.24 \qquad (2)$$

for $\mu = 0.6$, indicating that the gas and galaxies trace the potential with the same energy per unit mass and suggesting that the cluster core is not far from equilibrium.[11] To

compute the mass enclosed within 500 h^{-1} kpc, we follow the method of Wu (1994), which assumes an isothermal gas distribution. This approximation is reasonable, as the temperature profile of Abell 1651 is quite flat (Markevitch et al. 1998). Evrard, Metzler, & Navarro (1996) demonstrated in their simulations that isothermal β-models give an unbiased estimate of the true mass but also demonstrated that there is ∼20% scatter in the relation between the computed and true mass. With the isothermal assumption, the mass within a given projected radius, r_p, is computed as a function of β, T, a core radius r_c, and a "physical size" R for the cluster, which defines the line-of-sight depth over which to integrate the enclosed mass. For a projected radius of 500 h^{-1} kpc, the derived mass is only a weak function of r_c and R. For example, changing R from 3 to 8 h^{-1} Mpc modifies the resulting mass by 3%, while changing r_c from 20 to 100 h^{-1} kpc alters the resulting mass by 2%. This uncertainty is significantly smaller than the scatter from use of the isothermal model. For concreteness, we adopt $r_c = 50\ h^{-1}$ kpc and $R = 5\ h^{-1}$ Mpc. Including the scatter seen in the simulations, we compute

$$M(r_p < 500\ h^{-1}\ \text{kpc}) = (5.4 \pm 1.4) \times 10^{14}\ h^{-1}\ M_\odot\ . \quad (3)$$

The total *I*-band mass-to-light ratio within this region then is

$$M/L_I(r_p < 500\ h^{-1}\ \text{kpc}) = (160 \pm 45)h\ . \qquad (4)$$

A key point to note is the dependence of M/L_I on the inclusion of the extended BCG halo. Using only the BCG magnitude returned by SExtractor, we would have missed

---

[11] Girardi et al. (1998) claim that this cluster has significant substructure, in conflict with the derived value of β and detailed X-ray analysis (Markevitch et al. 1998). However, this finding is based on the distribution of a relatively small sample of 30 cluster galaxies.

50% of the light from the BCG and hence 18% of the cluster light. Consequently, if such extended halos are a generic feature of the brightest cluster galaxies, as they appear to be from our work and that of Uson et al. (1990, 1991) and Scheick & Kuhn (1994), then any M/L ratio that fails to account for this light will also overestimate M/L by $\sim 20\%$. This omission of luminosity exacerbates the cluster baryon problem for high-Ω_0 models (White et al. 1993).

5. FORMATION OF THE BCG HALO

What do the properties of the BCG tell us about the formation history of this system? We have found that the surface brightness profile of the BCG in Abell 1651 is, to first order, consistent with a de Vaucouleurs model and have observed that the profile becomes mildly redder with increasing radius. The uniformity of the profile over such a large radial range argues for early assembly of the extended halo.[12] Meanwhile, the color of the halo indicates that recently accreted cluster galaxies do not contribute a significant fraction of the halo luminosity and so also supports early formation.

These results are consistent with the recent work of Dubinski (1998). In his hydrodynamic cluster simulation, the BCG is assembled at $z \sim 0.8$ and significant accretion continues until $z \sim 0.4$, after which there are no major mergers involving the BCG. Dubinski finds that a brightest cluster galaxy with an $r^{1/4}$ profile out to $200 \ h^{-1}$ kpc is formed in this simulation via the merger of massive galaxies during filamentary collapse. He also notes that, as we observe in Abell 1651, "a cD galaxy envelope did not form in this system." In addition, the brightest cluster galaxy in the simulation retains a fossil alignment with the filament and the galaxy distribution. Such an alignment with the galaxy distribution and X-ray gas has been observed in real systems (Sastry 1968; Carter & Metcalfe 1980; Porter et al. 1991; Allen et al. 1995; Mulchaey & Zabludoff 1998). In Abell 1651 the BCG is aligned with both the X-ray gas contours (Fig. 8a) and, more marginally, with the distribution of confirmed cluster members obtained from NED (Fig. 8b). The alignment of Clump B with the BCG can also be interpreted in this picture as the recent disruption of a galaxy infalling along the direction of the filament.

6. SUMMARY AND CONCLUSIONS

We perform a detailed analysis of the distribution of luminous matter in the galaxy cluster Abell 1651. We assess the relative luminosity contributions of the brightest cluster galaxy, the rest of the cluster galaxy population, and any diffuse luminous matter in the cluster that is unassociated with the other two components. In the process we develop and demonstrate an approach for studying the distribution of luminous matter in cluster cores that allows detailed analysis but requires minimal telescope time (< 1 hr per cluster on a 1 m telescope). This technique can be applied to a large sample of clusters to test whether there exists true variation in the form of BCG surface brightness profiles and also whether intracluster light is a significant contributor in some systems.

In the case of Abell 1651, we find that the brightest cluster galaxy contains 36% of the total cluster light within $r = 500 \ h^{-1}$ kpc of the center of the BCG and the cluster. Furthermore, the profile of the BCG is well approximated by a de Vaucouleurs model out to $r = 670 \ h^{-1}$ kpc, which is consistent with it being a D-type galaxy (Matthews, Morgan, & Schmidt 1964; Morgan, Kayser, & White 1975; Schombert 1987). This radius is a significant fraction of the virial radius of the cluster ($2 \ h^{-1}$ Mpc; Girardi et al. (1998). Our current measurements extend farther in radius than those of Uson et al. (1990, 1991) for the cluster Abell 2029 and Scheick & Kuhn (1994) for Abell 2670, and we find close agreement with the results of these studies. We also detect a color gradient in the profile in the sense that the halo is redder than the core of the BCG. The properties of the brightest cluster galaxy are consistent with the scenario of filamentary collapse and formation of the BCG at high redshift, as evidenced by Dubinski's (1998) numerical simulations.

We constrain the luminosity of any additional diffuse matter in the cluster to constitute less than $\sim 5\%$ of the total luminosity. Furthermore, the residual flux observed is consistent with arising from cluster galaxies fainter than the magnitude limit of our data. Thus, diffuse light beyond that of the BCG profile is negligible for this system. We do detect one distinct patch of excess light along the semimajor axis of the BCG (region B) that appears to be truly diffuse light, possibly from a tidally disrupted galaxy. Two additional, fainter peaks in the surface brightness are also seen but are coincident with faint, clumped galaxies and have fluxes that are consistent with arising from these faint galaxies. The colors of these faint galaxies are consistent with the expected color of cluster dwarf ellipticals, and so a reasonable explanation is that these are groups of clumped cluster dwarfs. It is also possible that these galaxies are spirals in background clusters or groups.

Finally, we compute the I-band mass-to-light ratio and find $M/L_I = 160 \pm 45 \ h$. We note that failure to include the luminosity of the BCG halo causes M/L to be overestimated by 18%. If this halo profile is typical of BCGs, any study of cluster mass-to-light ratios that ignores this significant contribution to the cluster light will systematically overestimate M/L. Omission of this light will also induce a systematic bias in measurements of Ω_0 derived using the resultant mass-to-light ratios.

---

[12] The presence of oscillations in the profile also provides a potentially interesting constraint; however, dynamical modeling is first needed to assess the timescale over which such structure can be maintained in the cluster environment.

APPENDIX

The standard technique for fitting surface brightness profiles is via χ^2 minimization of the surface brightness data using the equation

$$\chi_v^2 = \frac{1}{N - M - 1} \sum_{i=1}^{N} \frac{(y_i - f_i)^2}{\sigma_i^2}, \tag{A1}$$

where χ_v^2 is the reduced χ^2, N is the number of data points, M is the number of free parameters, y_i is the measured flux at point i, f_i is the value of the functional fit at point i, and σ_i is the uncertainty in the flux. For a de Vaucouleurs model, there are three free parameters, r_e, Σ_e, and the sky level. Sersic models have n as a fourth free parameter. This approach is adequate for determination of r_e and Σ_e; however, fluctuations in the interior region of the galaxy (particularly correlated fluctuations arising from small-scale structure in the profile) have an inordinate impact on the resultant background level. For example, in our data for Abell 1651, determination of the sky level in this fashion leads to truncation of the profile beyond $r \sim 300 \ h^{-1}$ kpc, despite the fact that the surface brightness is observed to monotonically decrease to beyond $r = 600 \ h^{-1}$ kpc. For Sersic models, error in the background sky level also induces error in the derived n, and so this method provides little leverage on the form of the profile at large radii.

To avoid the ambiguity that arises from uncertainty in the background level, we have opted in this paper for a differential approach to determining the form of surface brightness profiles. A quick way to gain intuition for this approach is to plot the flux difference between adjacent data points ($\Delta f_i = f_i - f_{i+1}$) as a function of radius and compare this with various models. However, as discussed in the text, use of adjacent points has the drawback that χ_v^2, defined as

$$\chi_v^2 = \frac{1}{(N-1) - M - 1} \sum_{i=1}^{N-1} \frac{[(y_i - y_{i+1}) - (f_i - f_{i+1})]^2}{\sqrt{\sigma_i^2 + \sigma_{i+1}^2}}, \tag{A2}$$

is dependent upon the radial sampling density, and so it is not possible to determine the uncertainty in the derived parameters.

Instead, for each point in the profile we compute the average flux decrement between that point and all other points in the profile at larger radii. Mathematically,

$$\Delta f_i \equiv f_i - \frac{1}{N - i} \sum_{j=i+1}^{N} f_j. \tag{A3}$$

This internal referencing allows us to compute a mean χ^2 value for each point in the profile, with larger separations receiving larger weighting in determination of this mean value (because σ is roughly constant, while the flux decrement increases). The χ_v^2 equation for this method is

$$\chi_v^2 = \frac{1}{(N-1) - M - 1} \sum_{i=1}^{N-1} \left\{ \frac{1}{N-i} \sum_{j=i+1}^{N} \frac{[(y_i - y_j) - (f_i - f_j)]^2}{\sqrt{\sigma_i^2 + \sigma_j^2}} \right\}, \tag{A4}$$

with χ_v^2 now independent of sampling density. Because of the increased leverage at large radii, this method permits a more robust determination of n than is possible with the standard surface brightness fitting technique while yielding comparable values of r_e and Σ_e.

REFERENCES

Allen, S. W., Fabian, A. C., Edge, A. C., Bohringer, H., & White, D. A. 1995, MNRAS, 275, 741
Andreon, S., Garilli, B., & Maccagni, D. 1995, A&A, 300, 711
Bertin, E., & Arnouts, S. 1996, A&AS, 117, 393
Carter, D., & Metcalfe, N. 1980, MNRAS, 191, 325
Dalcanton, J. J. 1996, ApJ, 466, 92
de Vaucouleurs, G., & de Vaucouleurs, A. 1970, ApJ, 5, L219
Dubinski, J. 1998, ApJ, 502, 141
Evrard, A. E., Metzler, C. A., & Navarro, J. F. 1996, ApJ, 469, 494
Ferreras, I., Charlot, S., & Silk, J. 1999, ApJ, 521, 81
Franx, M., Illingworth, G., & Heckman, T. 1989, AJ, 98, 538
Garilli, B., Sangalli, G., Andreon, S., Maccagni, D., Carrasco, L., & Recillas, E. 1997, AJ, 113, 1973
Girardi, M., Giuricin, G., Mardirossian, F., Mezzetti, M., & Boschin, W. 1998, ApJ, 505, 74
Gonzalez, A. H., Zaritsky, D., Dalcanton, J. J., & Nelson, A. E. 2000, in preparation
Graham, A., Lauer, T. R., Colless, M., & Postman, M. 1996, ApJ, 465, 534
Gregg, M. D., & West, M. J. 1998, Nature, 396, 549
Gudehus, D. H. 1989, ApJ, 340, 661
Jarvis, J. F., & Tyson, J. A. 1981, AJ, 86, 476
Kauffmann, G., & Charlot, S. 1998, MNRAS, 294, 705
Larson, R. B. 1974, MNRAS, 166, 585
Mackie, G. 1992, ApJ, 400, 65
Malamuth, E. M., & Richstone, D. O. 1984, ApJ, 276, 413
Markevitch, M., Forman, W. R., Sarazin, C. L., & Vikhlinin, A. 1998, ApJ, 503, 77
Marleau, F., & Simard, L. 1998, ApJ, 507, 585

Matthews, T. A., Morgan, W. W., & Schmidt, M. 1964, ApJ, 140, 35
Melnick, J., Hoessel, J., & White, S. D. M. 1977, MNRAS, 180, 207
Merritt, D. 1984, ApJ, 276, 26
Morgan, W. W., Kayser, S., & White, R. A. 1975, ApJ, 199, 545
Mulchaey, J. S., & Zabludoff, A. I. 1998, ApJ, 496, 73
Oemler, A. 1973, ApJ, 180, 11
———. 1976, ApJ, 209, 693
Porter, A. C., Schneider, D. P., & Hoessel, J. G. 1991, AJ, 101, 1561
Sastry, G. N. 1968, PASP, 80, 252
Scheick, X., & Kuhn, J. R. 1994, ApJ, 423, 566
Schlegel, D. J., Finkbeiner, D. P., & Davis, M. 1998, ApJ, 500, 525
Schombert, J. M. 1986, ApJS, 60, 603
———. 1987, ApJS, 64, 643
———. 1988, ApJ, 328, 475
Sersic, J.-L. 1968, Atlas de Galaxias Australes (Cordoba: Obs. Astron.)
Simard, L. 1998, in ASP Conf. Ser. 145, Astronomical Data Analysis Software and Systems VII, ed. R. Albrecht, R. N. Hook, & H. A. Bushouse (San Francisco: ASP), 108
Uson, J. M., Bough, S. P., & Kuhn, J. R. 1990, Science, 250, 539
———. 1991, ApJ, 369, 46
Valdes, F. 1993, FOCAS User's Guide (Tucson: NOAO)
Vilchez-Gómez, R., Pelló, R., & Sanahuja, B. 1994, A&A, 283, 37
White, S. D. M., Navarro, J. F., Evrard, A. E., & Frenk, C. S. 1993, Nature, 366, 429
Wu, X. 1994, ApJ, 436, L115
Zaritsky, D., Nelson, A. E., Dalcanton, J. J., & Gonzalez, A. H. 1997, ApJ, 480, L91
Zaritsky, D., Schectman, S. A., & Bredthauer, G. 1996, PASP, 108, 104